The Astrophysical Journal, 637:811–822, 2006 February 1

THE CIRCUMSTELLAR STRUCTURE OF THE CLASS I PROTOSTAR TMC-1 (IRAS 04381+2540) FROM *HUBBLE SPACE TELESCOPE* NICMOS DATA

Susan Terebey
Department of Physics and Astronomy, 5151 State University Drive, California State University, Los Angeles, CA 90032; sterebe@calstatela.edu

David Van Buren
Jet Propulsion Laboratory, 4800 Oak Grove Drive, Pasadena, CA 91109; david.vanburen@jpl.nasa.gov

Michael Brundage
Microsoft Corporation, Redmond, WA 98052-6399

and

Terry Hancock
Anansi Spaceworks, Grandview, TX 76050
Received 2005 January 6; accepted 2005 September 27

ABSTRACT

The class I protostar TMC-1 (IRAS 04381+2540) is oriented favorably for determining the properties of its circumstellar envelope and outflow cavity. Deep, high spatial resolution *Hubble Space Telescope* (*HST*) NICMOS images at 1.6 μm exhibit both a narrow jet and a wide-angle conical outflow cavity. Model images of the scattered-light distribution fit the data well, reproducing the intensity level, cavity width, and observed limb brightening. The best-fit geometry for TMC-1 has a $45^\circ \pm 5^\circ$ source inclination and an $80^\circ \pm 5^\circ$ deprojected wind opening angle (full width). The age, normally a poorly known quantity, is well constrained; the protostar age, i.e., time since the onset of cloud collapse, is 1×10^5 yr to within a factor of 2. We offer a possible resolution to the well-known luminosity problem. By considering the efficiency of infall onto the protostar, we find that plausible parameters can give an efficiency, and hence accretion luminosity, as low as 10% of the value derived from the collapsing cloud core. The efficiency, together with a luminosity constraint, leads to a mass estimate that ranges from about 0.1 $M_\odot$ for high efficiency to 0.2 $M_\odot$ for low accretion efficiency onto the protostar. Similarly, the estimated mass accretion rate *onto the protostar* ranges over roughly $(0.9-1.4) \times 10^{-6}$ $M_\odot$ yr^{-1}, which is smaller than the $(1.6-3.5) \times 10^{-6}$ $M_\odot$ yr^{-1} infall rate *of the cloud*. If low efficiency rates are prevalent for protostars, one important consequence is that it will take longer to assemble the central star than the time $t = M_{\rm in}/\dot{M}_{\rm in}$, a time that assumes *all* of the infalling material lands on the protostar.

Subject headings: circumstellar matter — ISM: jets and outflows — stars: formation — stars: individual (TMC-1, IRAS 04381+2540)

Online material: color figures

1. INTRODUCTION

The Taurus molecular cloud, at a distance of 140 pc, is the nearest example of the isolated mode of star formation, in which dense cloud cores are well separated and generally form one or two stars. Sources in Taurus provide an important proving ground for testing star formation theories. A number of authors (Chandler & Richer 2000; Hogerheijde & Sandell 2000; Motte & André 2001) have modeled the structure of protostellar envelopes using dust continuum emission and conclude that for Taurus sources the structure is consistent with the predictions of what is sometimes called the standard star formation model (see references in Shu et al. 1987).

An alternative approach is to determine circumstellar structure using near-infrared observations of the scattered light in the protostellar envelope. Ground-based near-infrared imaging studies have established that the extended emission around protostars is primarily due to scattered light (Heyer et al. 1990; Kenyon et al. 1993b). Monte Carlo radiative transfer models have had good success in matching observed near-infrared images (Whitney & Hartmann 1993; Kenyon et al. 1993b; Whitney et al. 1997). The observed (bi)conical structure is produced by a combination of the infall envelope, the circumstellar disk, and the cavity evacuated by a bipolar outflow. Stellar photons traverse the outflow cavity and are then absorbed or scattered in the dusty disk or in the infall envelope. The resulting images reveal the $\tau \sim 1$ scattering surface, providing a direct way to measure the dust column and infer the density of the disk and infall envelope.

Scattered-light models have been fit to data for an increasing number of embedded sources (Kenyon et al. 1993b; Burrows et al. 1996; Whitney et al. 1997; Lucas & Roche 1998; Grosso et al. 2003; Wolf et al. 2003). In many cases the fits seem to provide a good match to the data. In some cases the results are limited by data quality, where insufficient dynamic range means the source geometry is not easily constrained. More often, sources with complicated structure are difficult to fit with a unique geometry. In addition, the large number of free parameters can make it difficult to assess the uniqueness of the fits.

In this paper we analyze high-quality *HST* Near-Infrared Camera and Multi-Object Spectrometer (NICMOS) images of TMC-1 (IRAS 04381+2540) at 1.6 μm to derive the underlying structure of the infall envelope and protostar outflow. We compute scattered-light models based on the Terebey et al. (1984, hereafter TSC84) cloud-collapse solution. The near-infrared appearance of TMC-1 exhibits a very regular structure that should provide an excellent test case for comparing cloud-collapse theory with observations of

TABLE 1
Source Parameters

Parameter	Value
IRAS/Core	IRAS 04381+2540/TMC-1
D	140 pc
L_{bol}	0.7 $L_\odot$
SED	I
R.A. (J2000)	$04^h41^m12^s.68$
Decl. (J2000)	$+25^\circ46'35''.4$
J	17.2 mag
H	14.14 mag
K_s	11.54 mag

Notes.—L_{bol} and SED in Bontemps et al. (1996); see also Chen et al. (1995). Position and photometry from 2MASS; the 2MASS position is recommended for absolute position reference.

a class I protostar. The source TMC-1 is one of about six *Infrared Astronomical Satellite* (*IRAS*) sources in the $\sim 1^\circ$ region known as Heiles cloud 2 in the Taurus molecular cloud. The high spatial resolution ($0''.15 = 22$ AU) and sensitivity of the data presented here supersede previous near-infrared images (Kenyon et al. 1993a; Chandler et al. 1996; Hogerheijde et al. 1998).

2. OBSERVATIONS

Table 1 shows source parameters for TMC-1. Near-infrared data were obtained for TMC-1 using the *HST* NICMOS camera in 1997 December. Using the Tiny Tim point-spread function (PSF) simulation program (Krist & Hook 1997), the FWHM size, weighted for the very red spectrum, is $0''.15$ for the F160W (1.60 μm) filter. Information from STScI showed that the NICMOS plate scale varied slowly with time after launch, such that the x and y NICMOS plate scales during the latter part of 1997 were $0''.0761$ pixel^{-1} and $0''.0754$ pixel^{-1}, respectively. The spatial resolution thus corresponds to about 2 pixels, while the chip size of 256×256 implies a $19''.4$ field of view. Furthermore, we constructed an empirical NICMOS PSF by clipping a star from our other NICMOS data (Terebey et al. 2001).

We obtained two long exposures (2×1280 s) that were dithered by $1''.5$ and co-added in postprocessing, where one frame was down-weighted due to its high noise. Data reprocessing used the *HST* reduction software CALNICA version 3.0 (Casertano et al. 1997). The standard flat field provided by STScI left a residual flat-field signature in the image, which was eliminated using the following technique. The NICMOS sensitivity has fixed spatial appearance but is strongly wavelength dependent, appearing most uniform at the longest wavelengths. Therefore, existing STScI flat fields overcorrected the red protostar image. The flat field was modified using a power-law transformation on the pixel values V_i^p, followed by image renormalization. The power-law index $p = 0.8$ was best at eliminating the flat-field signature from the image.

The noise σ_n is 0.014 μJy pixel^{-1}, leading to a dynamic range of about 2000:1 in the reduced broadband images. We note that the intensity values are systematically negative around the periphery of the image, indicating that there is a small uncertainty in the NICMOS zero-level calibration. In principle, we could have solved for the value of the offset in the χ^2 fit (§ 4.5), but in practice, adding a small arbitrary offset made too small an improvement to justify adding a free parameter to the fitting procedure.

The orientation of the raw data has north at position angle (P.A.) $= 123^\circ.6$, as given by the ORIENTAT keyword in the supplied FITS header. To realign north to P.A. $= 0^\circ$, the image was resampled, magnified by a factor of 6, rotated around the star position, then resampled back to the original pixel size.

3. TMC-1/IRAS 04381+2540: JET SOURCE WITH WIDE-ANGLE WIND

The *HST* NICMOS data show that TMC-1 (Fig. 1) has extended emission covering most of the field of view; the lowest intensity levels define a striking wide-angle conical reflection nebulosity (one-sided), where the central star is seen at the southern apex. Previous near-infrared and CO data show a wide-angle biconical outflow that extends north-south; the derived inclination is 40°–70° (Chandler et al. 1996). Near-infrared scattering models predict the one-sided shape for moderate-inclination sources (Whitney & Hartmann 1993); the blueshifted northern lobe is nearer and hence clearly visible, while the redshifted southern lobe is farther away and completely extincted by the intervening infall envelope and/or circumstellar disk.

A well-defined jet extends nearly $4''$ north from the source. Presumably, the emission is due to [Fe II] line emission at 1.64 μm contained within the F160W passband. The jet appears unresolved in the perpendicular direction at $0''.15$ resolution. The jet is not perfectly straight; a line drawn back toward the source does not point directly toward the protostar, but rather it is in between the protostar and the bright neighboring cometary clump. It is possible that the comet-shaped clump represents a second embedded star, but these data are not conclusive.

Despite the large numbers of known jet sources and molecular outflow sources, there are few examples of young stars simultaneously showing both wide-angle outflows and jets. Exceptions are the prototypical source L1551-IRS 5 (Davis et al. 1995), and possibly the source FS Tau B (Eisloffel & Mundt 1998). However, due to confusion with a nearby star, the spectral energy distribution and classification of FS Tau B are not well known. By contrast, TMC-1 is isolated and well characterized as a typical class I protostar. It provides an interesting example of a source that simultaneously connects a jet with a wide-angle outflow.

4. RADIATIVE TRANSFER MODELS

Following the approach of Whitney and collaborators (Whitney & Hartmann 1993; Whitney et al. 1997, 2003), we used a Monte Carlo code to model the radiative transfer of the stellar photons that scatter through the dusty circumstellar material. In particular, we compare results with Whitney & Hartmann (1993, hereafter WH93). The adopted density distribution has three components: outflow, envelope, and disk. The density model is similar to the "streamline" model of WH93, in which the boundary of the outflow cavity follows a streamline of the TSC84 infall solution. The motivation is that their streamline models look similar to our data. The streamline naturally provides a conical shape for the outflow cavity at large distances from the disk, such that the semiopening angle of the wind, θ_w, approaches a constant value. In the case of TMC-1 the assumption of zero optical depth within the outflow cavity turns out to be sufficient. For the infall envelope density we use the full TSC84 solution, whereas the one used by WH93 is identical to the inner limit of the TSC84 solution: the two envelope distributions diverge at scales larger than the disk size, i.e., $\gtrsim 1000$ AU in radius. The disk is assumed to be opaque and infinitesimally thin with an inner dust-free hole. When comparing with WH93, who assumed no inner hole, we applied an inclination-dependent intensity correction along the line of sight to the star, because the optically thick disk blocks the observer's view of the star below the disk midplane. We set the outer disk radius equal to that implied by the collapse solution, the radius of which is controlled by the angular momentum of the infalling material. The

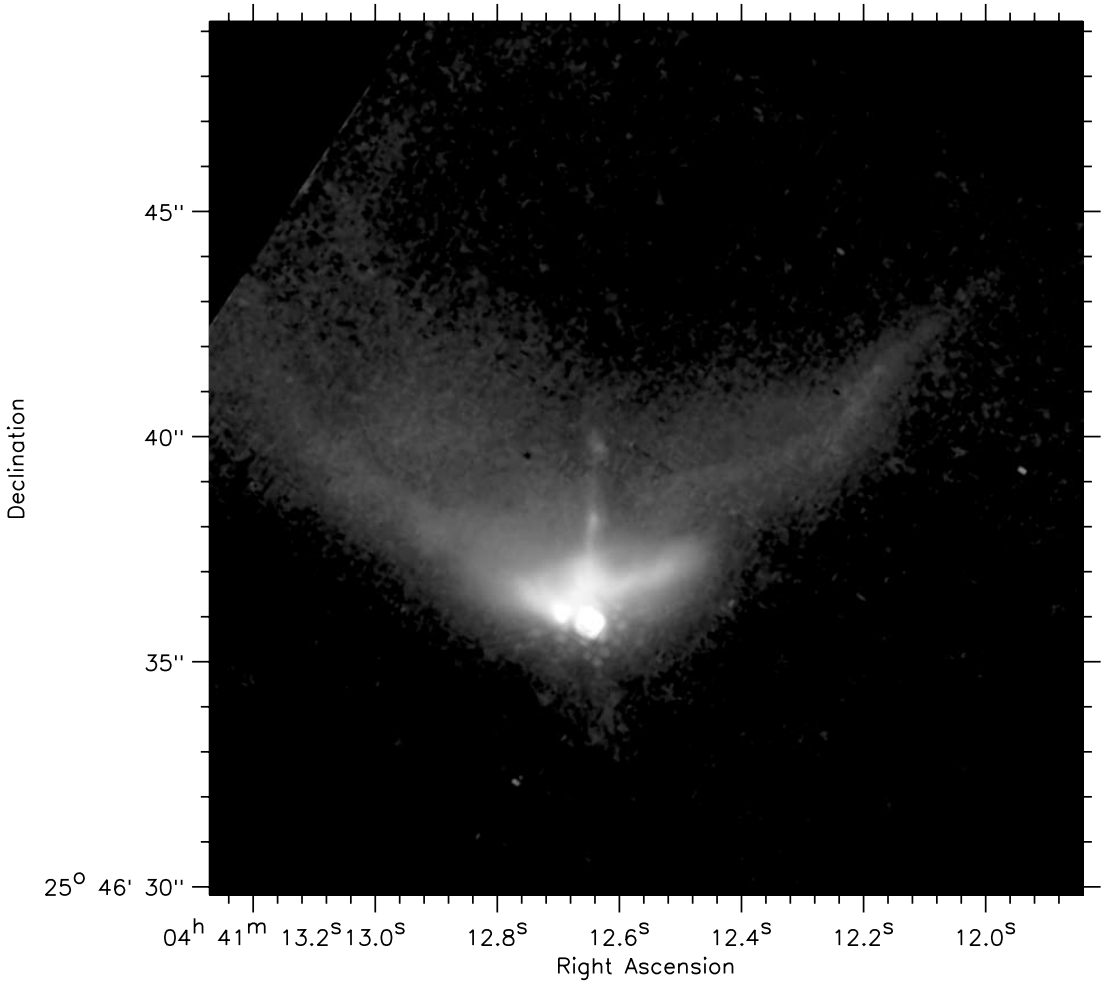

FIG. 1.—Circumstellar nebulosity around the protostar TMC-1 at 1.6 μm outlining the walls of a low-density outflow cavity. Bisecting the outflow is a narrow jet. The jet emanates north from the unresolved protostar (NICMOS diffraction pattern). The image is 19″.4 on a side, gray = 1.6 μm, log stretch. The resolution is 0″.15 = 21 AU at the 140 pc distance. [*See the electronic edition of the Journal for a color version of this figure.*]

opaque disk has little direct effect on the scattered-light models presented here; its significance is that the radius r_d sets the scale for which the infall envelope is noticeably flattened rather than spherically symmetric. Our disk model is simple but adequate for studying young envelope-dominated sources (class I) that are not seen edge-on, i.e., have $i < 70^\circ$ source inclination.

The radiative transfer code `rt` was written in C++ in two dimensions, using an adaptive grid based on cylindrical coordinates. The code outputs a list of photon escapes, including position and direction, which are in turn fed to visualization code `rt_vis` to produce a simulated image. The simulation space comprises a cylinder centered on the star, having radius R, and also height $\pm R/2$ with respect to the equatorial midplane. To better compare with the NICMOS data, we convolved the model image with a NICMOS PSF.

We tested the code by comparison with model 7 of WH93, run for the same parameters, and accounting for the different treatment of the inner disk hole. Comparison of the simulations by overlaying the images showed that the contour lines were essentially identical. Additional testing showed a gridding artifact, namely, "rings" that are visible in the model images. The rings are a model artifact due to the boundary between the outflow cavity (assumed to have zero density) and the opaque envelope. The outflow cavity is roughly conical at a large distance, whereas the model grid is cylindrical; hence, a photon traveling radially outward from the star encounters a "stair-step" grid in the optical depth near the outflow/envelope interface. Introducing a smoother transition in density across the interface would mitigate the artifact. However, implementing an improvement to the `rt` code is deferred to the future, as the model artifact does not materially change the conclusions presented in this paper.

4.1. *Density and Opacity*

The Monte Carlo technique propagates photons through the cloud in response to the optical depth increment $d\tau$, where

$$d\tau = \kappa \rho \, dl, \tag{1}$$

and where κ is the specific dust opacity, dl is the increment in path length, and ρ is the gas density. The simulation is carried out in nondimensional coordinates that are natural to the TSC84 solution. Starting with spherical coordinates (r, θ, ϕ), time t, the isothermal sound speed in the cloud a, and initial angular rotation rate of the cloud Ω, the nondimensional radius is given by $x = at$, and nondimensional time $T = \Omega t$. The range $x < 1$ defines the region undergoing collapse (i.e., infall). The density of the cloud core (also called the infall envelope) is given by

$$\rho = \frac{\alpha(x,\ T,\ \theta)}{4\pi G t^2}, \tag{2}$$

where G is the gravitational constant and $\alpha(x,\ T,\ \theta)$ has the form specified by the TSC84 collapse solution. The TSC84

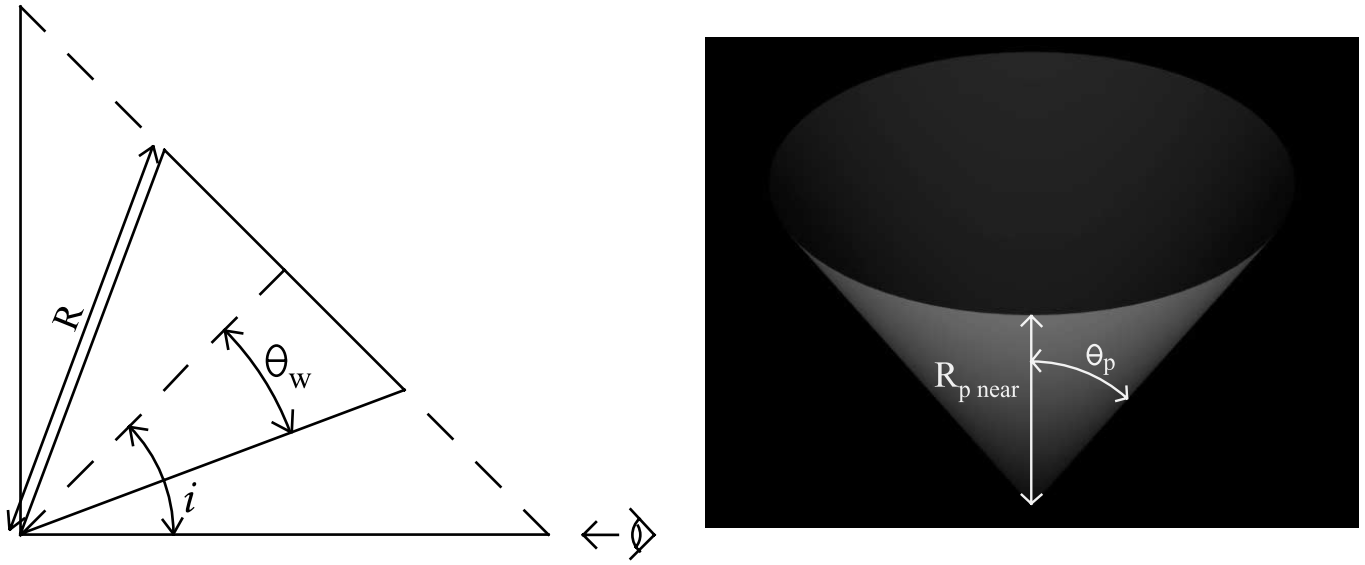

FIG. 2.—*Left*: The schematic of the adopted outflow geometry shows a biconical outflow cavity that is inclined toward the observer. The observer is looking almost tangentially along the wall of the outflow cone. *Right*: The view in the plane of the sky. The projected rim of the outflow cone corresponds to a similar feature in the TMC-1 image (Fig. 1) for the near side of the outflow cone. [*See the electronic edition of the Journal for a color version of this figure.*]

solution is completely specified using three parameters—a, Ω, and t—which can be alternately expressed as the three parameters $\dot{M}_{\rm in}$, $M_{\rm in}$, and r_d, where $\dot{M}_{\rm in} = 0.975a^3/G$ is the constant mass infall rate into the inner region (disk plus star), $M_{\rm in} = \dot{M}_{\rm in}t$ is the inner mass, and $r_d = a\Omega^2 M_{\rm in}^3/2\dot{M}_{\rm in}^3$ is the disk radius. Notice that both the mass and disk radius increase with time as the collapse proceeds.

We reexpress the equation for optical depth in terms of nondimensional path length $L = l/at$ and expand the density ρ to give

$$d\tau = \sigma(T)\alpha(x,\ T,\ \theta)dL, \tag{3}$$

where by definition, $\sigma = a\kappa/4\pi Gt$ or, equivalently,

$$\sigma = \frac{1}{4\pi G^{2/3}(0.975)^{1/3}}\kappa\dot{M}_{\rm in}^{-2/3}M_{\rm in}, \tag{4}$$

$$T = \frac{2^{1/2}(0.975)^{1/6}}{G^{1/6}}r_d^{1/2}\dot{M}_{\rm in}^{1/3}M_{\rm in}^{-1/2}. \tag{5}$$

Using this formulation means that two nondimensional parameters, σ and T, are needed to compute a model, and that model applies to the family of $M_{\rm in}$, $\dot{M}_{\rm in}$, and r_d that have the corresponding σ- and T-values.

4.2. *Dust Model*

Dust properties control the scattering of photons at near-infrared wavelengths. For our baseline dust model, we adopt that of Kim et al. (1994), having $\kappa = 40$ cm^2 g^{-1} opacity, $\omega = 0.41$ albedo, and a $g = 0.28$ forward-scattering parameter for $R_V = 3.1$ at 1.6 μm dust ($R_V = 5.3$ "dense cloud" dust is similar). Their mixture contains some micron-size grains, which serve to keep the values of κ and g high enough at 1.6 μm to fit our data.

4.3. *Intensity Scale*

The nominal units of the model image were the number of simulated photons per steradian. To convert to physical units we adopt a protostellar flux at 1.6 μm of 0.325 Jy for 140 pc distance. Model intensities will scale directly with the adopted central flux. Protostar parameters are not well known, but for comparison, a blackbody having $T = 3000$ K and $R_* = 3\ R_\odot$ (e.g., Stahler 1988) gives the assumed 1.6 μm flux and matches the 0.7 $L_\odot$ bolometric luminosity (Fig. 1) of TMC-1. If the luminosity is dominated by accretion, then the assumed 1.6 μm flux is reasonable if the accretion energy is thermalized; i.e., the optical depth is high. Our adopted flux is functionally equivalent to WH93; their standard parameters for T Tauri stars, $T = 4000$ K and $R_* = 2\ R_\odot$, lead to an intensity scale that is identical at this wavelength.

4.4. *Outflow Geometry*

Figure 2 shows a schematic diagram of the outflow geometry for a source with inclination i, where $i = 90^\circ$ corresponds to an edge-on disk. As discussed in Chandler et al. (1996), the relation between the wind semiopening angle θ_w and the apparent opening angle θ_p for an inclined cone projected onto the plane of the sky is given by

$$\tan\theta_w = \tan\theta_p \sin i. \tag{6}$$

In addition, if the outflow cone has length R, then the near side of the outflow cone has a projected length of $R_{p,\rm near}$, given by

$$R_{p,\rm near} = R\sin(i - \theta_w), \tag{7}$$

TABLE 2
SOURCE PARAMETERS FROM NICMOS DATA

Parameter	Value
θ_p[a]	50°.0
$R_{p,\rm near}$[b]	4″.2
P.A.$_{\rm wind}$[c]	4°.0
P.A.$_{\rm jet}$[c]	−1°.0

[a] The apparent semiopening angle of the wind/outflow.
[b] The near side of the outflow cone, projected onto the plane of the sky.
[c] The position angle in degrees E of N for the wind and jet, respectively.

TABLE 3
DEPROJECTED WIND OPENING ANGLE AND CLOUD RADIUS VERSUS INCLINATION FOR $\theta_p = 50^\circ$, $R_{p,\mathrm{near}} = 4''.2$

i (deg)	θ_w (deg)	$i - \theta_w$ (deg)	R (arcsec)
40.0	37.5	2.5	96.0
45.0	40.1	4.9	49.0
50.0	42.4	7.6	32.0
55.0	44.3	10.7	23.0
60.0	45.9	14.1	17.0

while the far-side projected length is

$$R_{p,\mathrm{far}} = R \sin(i + \theta_w). \quad (8)$$

These equations implicitly assume that the outflow has a circular cross section rather than one that is elliptical or some other shape. Deviations from a circular cross section modestly increase the uncertainty in the fitted outflow parameters, as long as the asymmetry is not too great.

Examination of the source structure (Fig. 1) permits us to estimate several parameters directly from the image. The northern outflow lobe has a constant projected opening angle $\theta_p = 50^\circ$, accurate to a few degrees, except in the region closest to the star. Notice a faint but distinct elliptical rim that lies north of the central source; we interpret this as showing that the outflow has a sharp outer boundary, similar to the ellipse formed by projecting outflow length R in the schematic diagram (Fig. 2). Across the rim the intensity jumps by a factor of 2 over a distance roughly equal to the PSF, too sharp to be a $\tau = 1$ transition in column density. Hence, we treat the rim feature as an outer cloud boundary. We measure $R_{p,\mathrm{near}} = 4''.2$, with an uncertainty of about 10% due to variations in the rim edge. In this interpretation, the view toward the protostar has the observer looking down/along the wall of the outflow cavity. An important consequence of this geometry is that the outer cloud boundary is seen, in projection, as a rim that is highly foreshortened. Table 2 gives the source parameters that are estimated from the data.

To summarize, the constraint $\theta_p = 50^\circ$ when combined with equation (6) gives a family of solutions that relate source inclination to the appropriate deprojected wind opening angle. Also, given the source inclination, the constraint $R_{p,\mathrm{near}} = 4''.2$ can be deprojected to give R, the cloud outer radius. Applying these constraints to TMC-1, Table 3 gives the deprojected opening angle and cloud-core radius for a range of plausible inclination angles. The visual impression from the data that the observer's sight line to the star is directed tangentially down/along the wall of the outflow cavity is the condition that $i - \theta_w \sim 0^\circ$, which Table 3 shows is approximately satisfied for this source.

4.5. *Parameters*

We summarize the free parameters so far discussed:

1. Intensity and pixel scale: the stellar flux F at 1.6 μm and distance D.
2. Dust properties: κ, ω, and g at 1.6 μm.
3. Density parameters: σ, T, and r_d for the TSC84 solution.
4. Geometric parameters: inclination i, wind θ_w, and cloud radius R.

In earlier sections, values were adopted for F, D, κ, ω, and g: the stellar and dust parameters. In addition, the geometric parameters are constrained by the TMC-1 data (§ 4.4), collapsing the free parameters from three to one, the source inclination. Finally, the simulations are solved in nondimensional form, which reduces the number of density parameters from three to two. The reduced set of parameters to be fit for the TMC-1 data is:

I. Density parameters: σ and T, for the TSC84 solution.
II. Geometric parameters: inclination i.

We find a best-fit model by varying the three parameters i, σ, and T to minimize the reduced χ^2 value. Additional tests to determine

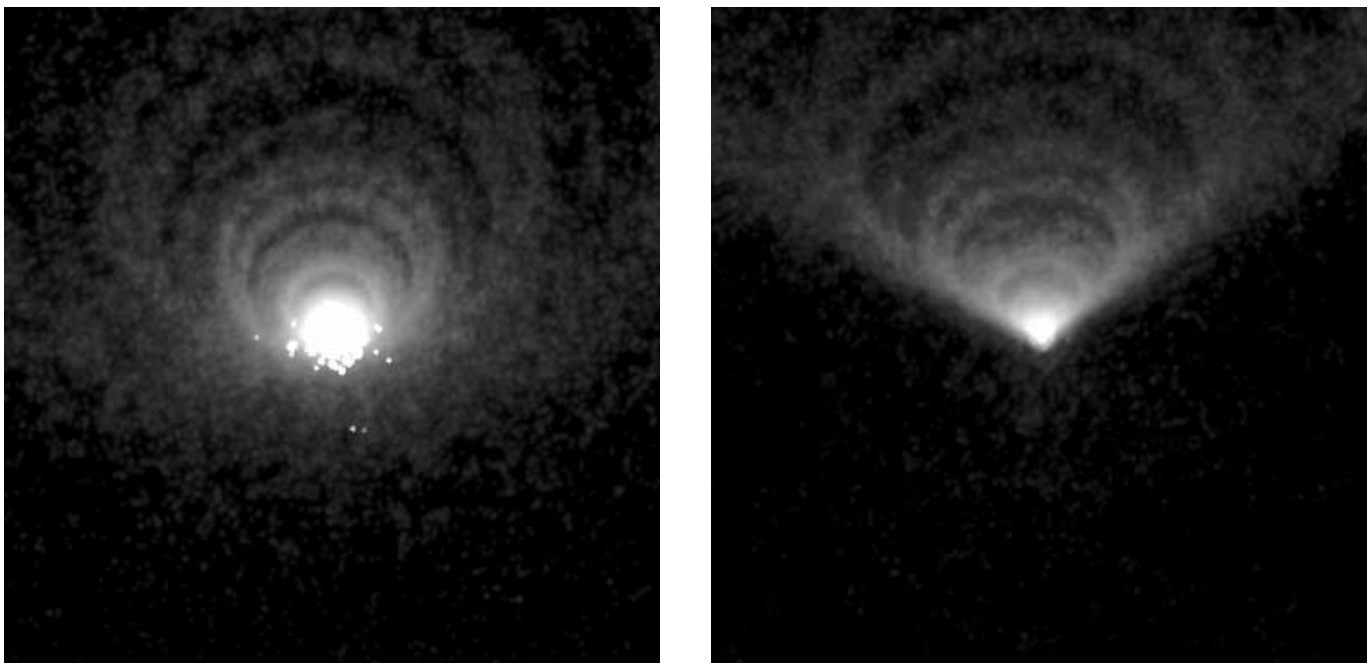

FIG. 3.—Effects of source inclination. *Left*: 30° inclination. The stellar PSF dominates at low inclinations. *Right*: 45° inclination. The image size is 19″.4, same as Fig. 1. Note that the apparent "rings" in the images are not real but are due to a model artifact (§ 4). [*See the electronic edition of the Journal for a color version of this figure*.]

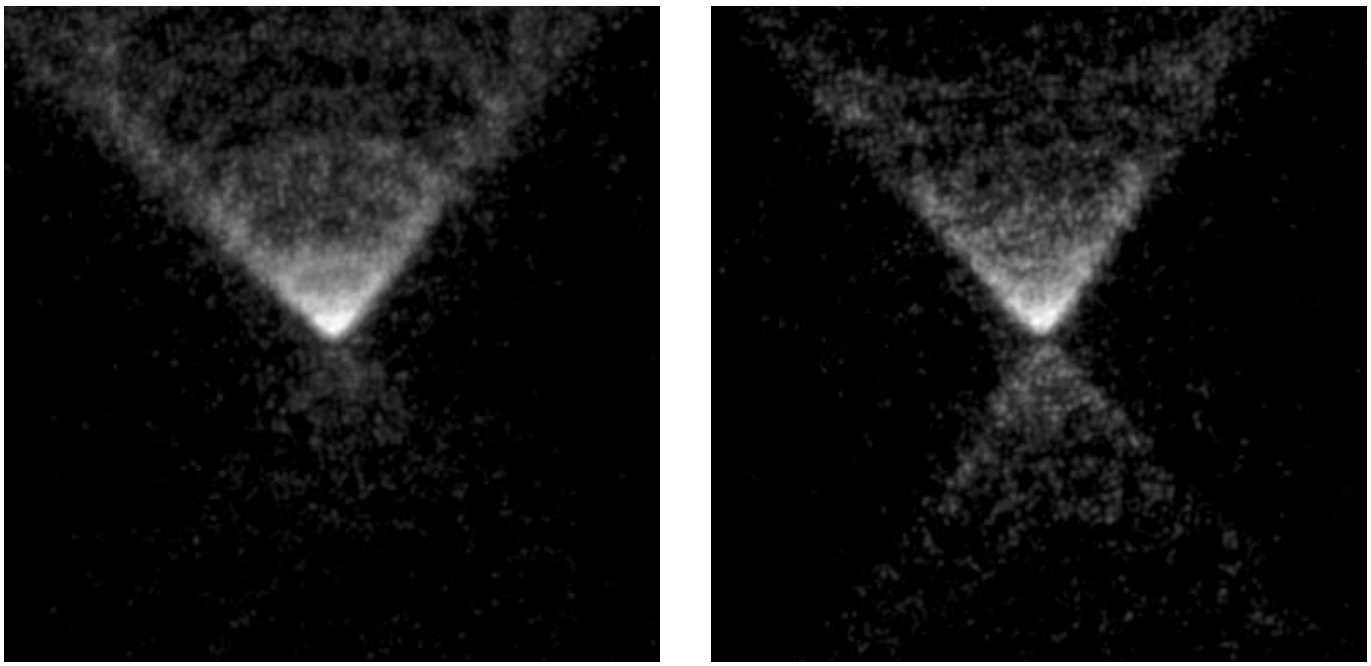

FIG. 4.—Effects of source inclination. The left and right panels show 60° and 75° inclinations, respectively. The image size is 19.″4, same as Fig. 1. Both outflow lobes become visible at high inclination, but the PSF-like protostar disappears. At high inclinations the disk (80 AU = 0.″5) is barely seen as a small and narrow absorption lane just below the star. [*See the electronic edition of the Journal for a color version of this figure.*]

how sensitive the χ^2 value was to changes in other parameters showed that χ^2 was most sensitive to i, σ, and T, whereas $\sqrt{2}$ changes in cloud radius R and dust properties ω and g produced much smaller effects.

4.6. *Effect of Inclination on Source Morphology*

The morphology of the scattered light depends on source inclination, particularly when $\tau \gtrsim 1$ in the envelope (WH93). The models in Figures 3 and 4 illustrate this effect for TMC-1. First, note how the apparent wind opening angle becomes greater than the true wind opening angle at low inclinations (§ 4.4), due to projection effects. The figure also shows three different morphologies, related to whether one or both outflow lobes are visible. At low inclinations, i.e., near pole-on, the observer looks through the evacuated outflow cavity and the star is clearly seen, surrounded by nebulosity that is orders of magnitude fainter. At intermediate inclinations the nearer (northern) outflow cone is visible, while the farther (southern) outflow cone is completely extincted by the intervening envelope (plus disk) material. At high inclinations the bipolar shape becomes visible, and the disk signature is a narrow dark absorption lane close to the star. Note that the apparent "rings" in the images are not real but are due to a model artifact (§ 4).

4.7. *Data Comparison with Models*

The morphology seen in the TMC-1 image (Fig. 1) compared with Figures 3 and 4 immediately suggests that the source is seen neither pole-on nor edge-on but at intermediate inclination. The central star appears as an unresolved point source, while the lower outflow cone is invisible; this further suggests that the inclination is near the minimum value of the possible range (WH93). The source structure is understandable (Fig. 2) if the observer's sight line to the star is directed tangentially down/along the wall of the outflow cavity. The source TMC-1 exhibits a narrow jet extending north from the central region. In this paper we do not attempt to reproduce the jet emission.

Figure 5 shows the best-fit model, determined by finding the minimum reduced χ^2 value in a grid of models. Table 4 gives parameter values for the best-fit model and model suite. Apart from the jet, the model successfully reproduces the main features of the data. The model and data exhibit the same projected opening angle, the central star is visible, the lower outflow cavity is not seen, and the overall intensity level is the same, in both the

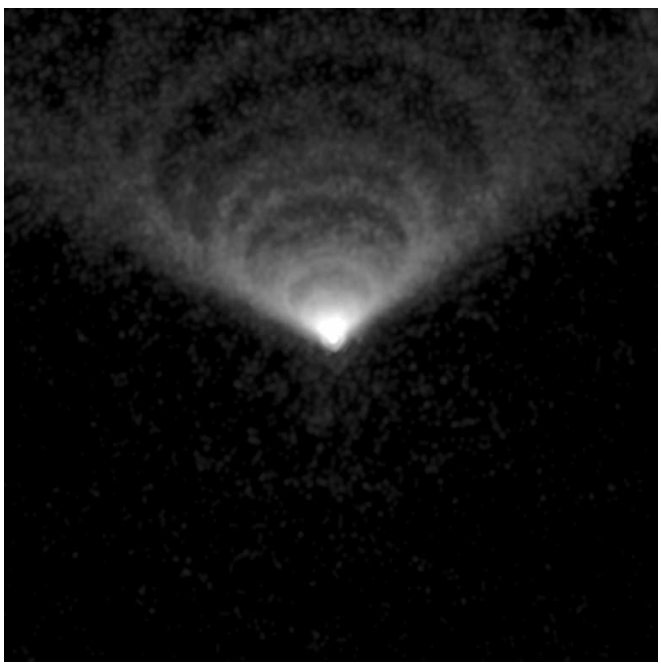

FIG. 5.—Best-fit model: $i = 45°$, $\theta_w = 40°$, and age $t = 10^5$ yr; other parameters are described in the text. Kim et al. (1994) dust with $R_V = 3.1$ at 1.6 μm has $\kappa = 40$ cm^2 g^{-1} specific opacity, $\omega = 0.41$ albedo, and a $g = 0.28$ scattering parameter. The image size is 19.″4, same as Fig. 1. [*See the electronic edition of the Journal for a color version of this figure.*]

TABLE 4
PARAMETER VALUES FOR MODEL GRID

Parameter	Best Fit	Minimum	Grid Step	Maximum
i	45.0	40.0	+5.0	60.0
σ	0.420	0.148	$\times\sqrt{2}$	1.19
T	0.117	0.021	$\times\sqrt{2}$	0.331

bright central regions and the faint outer regions. Figures 6 and 7 compare the intensity profile of the data and model in two representative annuli centered on the star. Note that the intensity scale is different for the two annuli by a factor of about 5, indicating in fact that the data and model intensity track each other well at different radii. The profiles show that the edges of the outflow cavity (P.A. $= -50^\circ$ and 50°) are sharp, indicating high optical depth in the envelope so that most photons are absorbed or scattered near the outflow/envelope boundary. Moreover, the outflow profiles show "horns" that signify limb brightening, which we discuss momentarily. For the data, the intensity outside the outflow cavity achieves a very low value, including the region covering

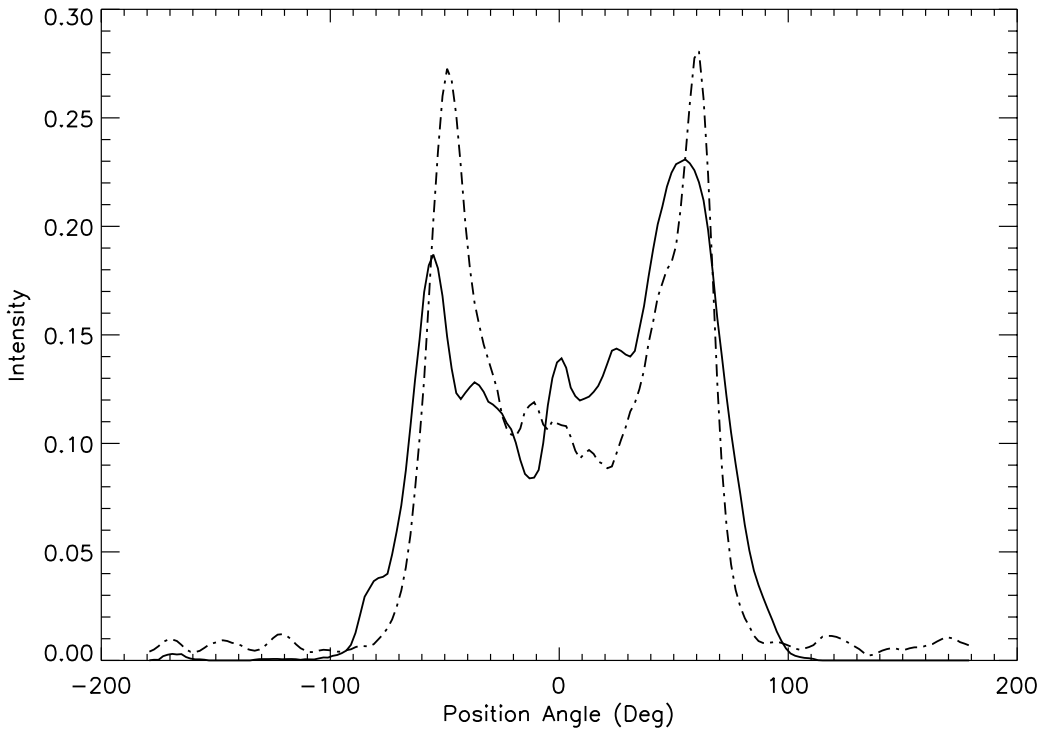

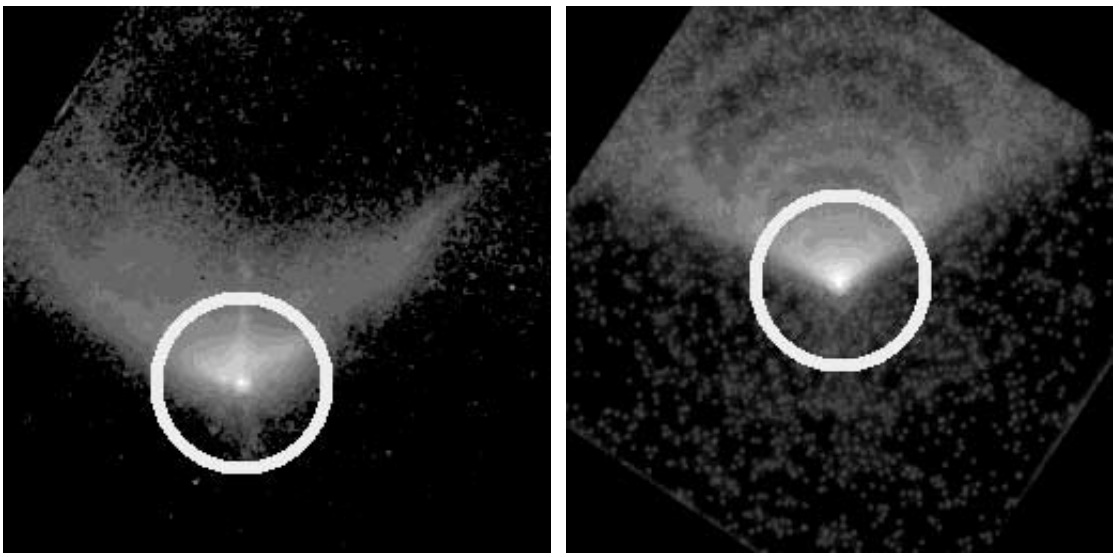

FIG. 6.—Good fits achieved for intensity vs. position angle. Plotted in the top panel is the model intensity (*dot-dashed curve*) vs. TMC-1 data (*solid curve*) for an annulus with 3″ radius. The profile samples the projected near wall of the outflow cone. The observed steep-sided profile (P.A. $= 50^\circ$ and -50°) of the projected outflow cavity implies that the envelope is optically thick so that photons are scattered in a thin layer that traces the outflow-envelope interface.

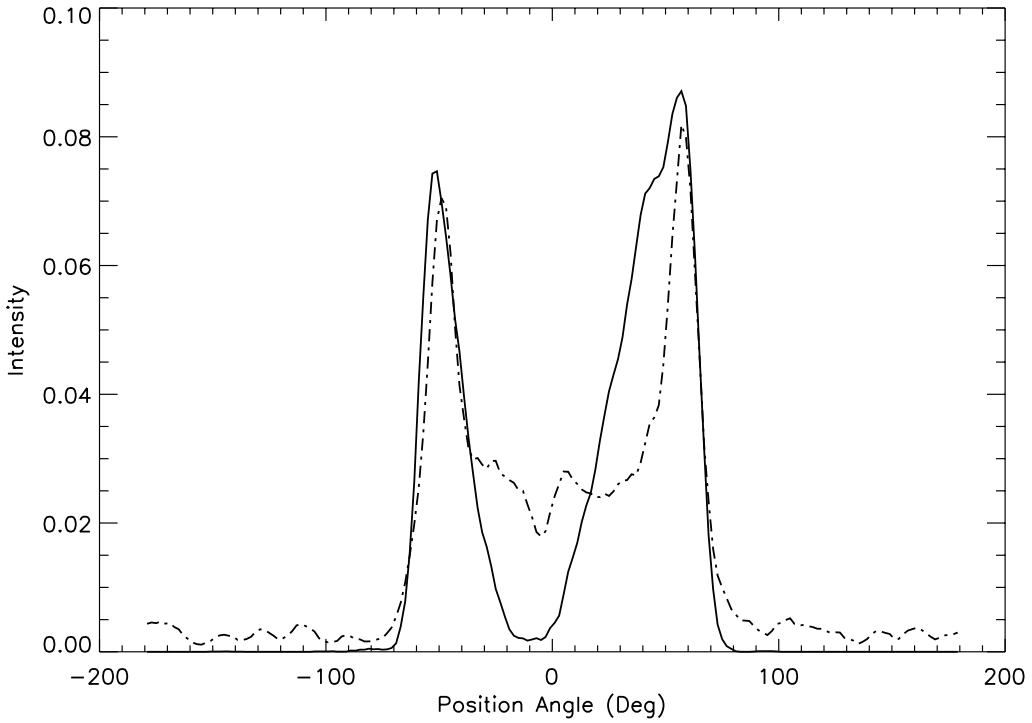

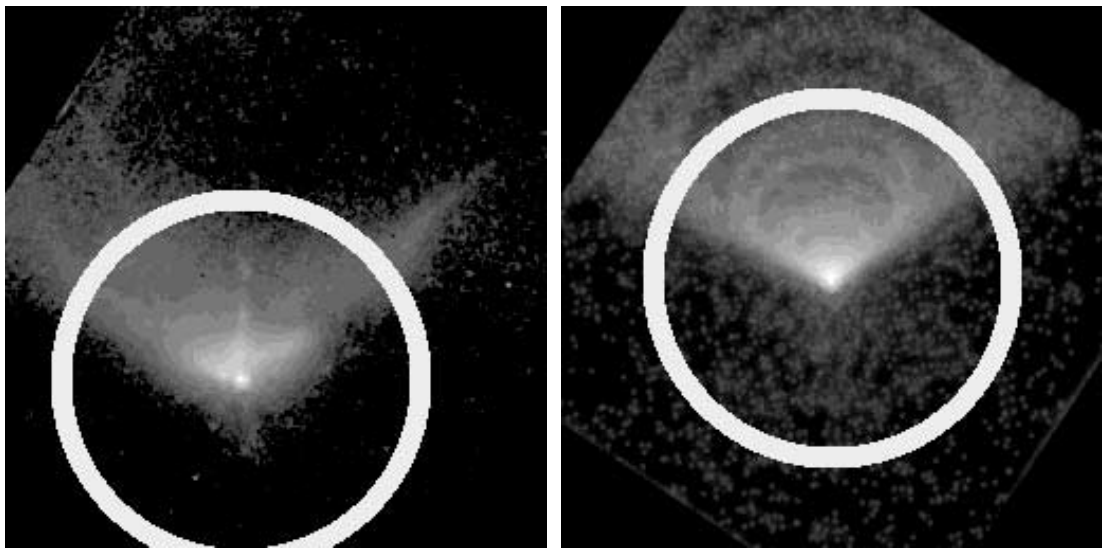

FIG. 7.—Intensity vs. position angle for an annulus with 6″.4 radius sampling the far wall of the outflow cone. The top panel shows model intensity (*dot-dashed curve*) vs. TMC-1 data (*solid curve*). Outside $\gtrsim 5''$ radius, the intensity profiles exhibit strong limb brightening.

the southern outflow lobe; the models generally predict more scattered light in the dark regions.

The intensity profiles have a different character at radii smaller or larger than 4″.2, the edge of the projected (and highly foreshortened) near side of the outflow cone (§ 4.4). The angular intensity profile located at 3″ from the star (Fig. 6) traces the *near side* of the outflow cone only. For this and similar radii, the contrast ratio between the edge and center of the outflow (ignoring the jet emission) is modest, less than a factor of 2. By comparison, the outer of the two profiles at radius 6″.4 (Fig. 7) traces only the *far side* of the outflow cone. For large radii the observed contrast ratio between the outflow center and edge is high, as high as 20:1. We find that the observed high contrast ratio in the data provides a strong constraint on the models. Most combinations of inclination and opening angle lead to angular profiles that trace the near side of the outflow cone and hence exhibit modest limb brightening. The dust behavior also affects scattering, so we investigated the effects of changing g to emphasize the forward-/back-scattering asymmetry. The decreased scattering efficiency at scattering angles $\sim 90^{\circ}$ due to large g-values indeed led to lower intensity from the far side of the outflow cavity, but the decrease was not enough to produce the observed high contrast ratios. The only combination of model parameters that led to high limb brightening was the geometric constraint we present in this paper: high limb brightening corresponds to an intensity profile that traces the *far side* of the outflow cavity.

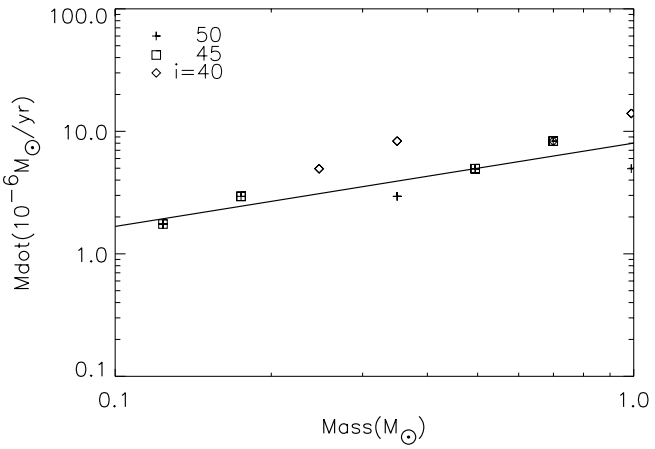

FIG. 8.—Cloud infall rate and inner mass, correlated for models that give an acceptable fit. Applying an independent luminosity constraint suggests that inner masses above 0.3 $M_\odot$ can be ruled out. The solid line shows the relation $\dot{M}_{\rm in}/(5 \times 10^{-6}\ M_\odot\ {\rm yr}^{-1}) = (M_{\rm in}/0.5\ M_\odot)^{0.68}$. Acceptable models have varying disk radii, as described in the text.

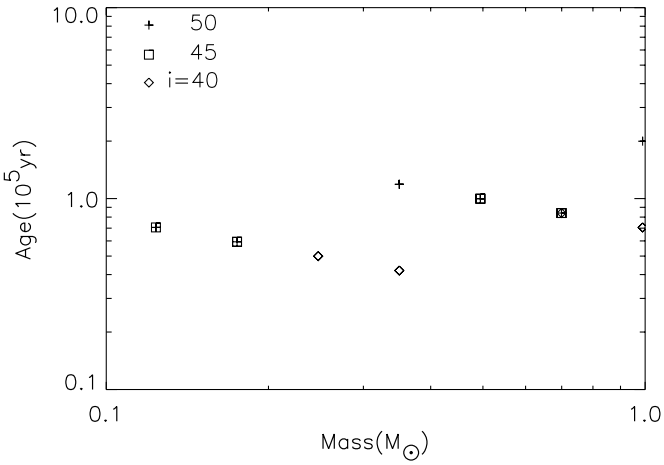

FIG. 9.—Age $\dot{M}_{\rm in}/M_{\rm in}$, i.e., time since the onset of cloud collapse, independent of inner mass for models with an acceptable fit, having a value of 1×10^5 yr to within a factor of 2.

Overall, the TMC-1 data are reasonably fit with an axisymmetric density model; however, the data exhibit significant inhomogeneities. The jet emission is close to but not exactly aligned with the central axis of the outflow cavity, its position angle differing by about 5°. In the central region there is a bright clump of emission east of the protostar. The angular intensity profiles are not mirror symmetric (Fig. 7); the eastern side of the outflow lobe is significantly brighter than the western side. In particular, the outer profile shows a gap in the emission where the intensity drops well below the model prediction. As previously discussed, varying the dust properties did not reproduce the large limb brightening and low emission level. We conclude that the low-intensity region reflects density rather than dust variation, caused by a lack of scattered photons, which in turn is due to very low density in the envelope at the *far side* of the outflow cavity. The material in the far wall may be missing due to nonaxisymmetric structure such as changes in the cloud edge or in the outflow shape.

4.8. *Parameter Uncertainties*

Previous work that compares Monte Carlo scattering models with data has focused on finding best-fit models, but has not addressed the issue of uniqueness. Here we consider the issue of finding acceptable fits. The method is based on using the reduced χ^2 value in a grid of models to estimate the uncertainty in the best-fit parameters (Table 4). The variable χ is just $(d_i - m_i)/\sigma$, defined to measure the difference between the data d_i and model m_i for each (independent) pixel, measured in units of σ, the noise. A standard way to proceed would be to compute χ^2 surfaces over a grid of models to define confidence intervals. This approach was too computationally intensive, so we adopted a more qualitative approach.

The intensity profiles in Figures 6 and 7 illustrate the difficulty of fitting high-quality astronomical images. The deviations of the data from the model are seen to be much larger than the random noise σ_n of the data and trace real differences in source structure between the data and model. Given that the image spatial resolution corresponds to about 2 pixels, there are roughly $128 \times 128 \sim 10^4$ independent data samples; in principle, we could improve the fit by increasing the number of free parameters in the model. However, this is not a satisfying approach, as much of the variation apparent in Figures 6 and 7 appears to trace small-scale structure variations rather than low-frequency smooth components that could be related to a physical model. We proceed by treating the structure variations as an additional source of noise in the data, rather than by trying to improve the fit in an ad hoc fashion by increasing the number of free parameters in the model.

The structure noise $\sigma_{\rm struct}$ is estimated by, in essence, renormalizing the reduced χ^2 value to be 1. First we assume $\sigma = \sigma_n$ so that the noise is just the random noise; the minimum reduced χ^2 is then about 12 for our best-fit model. Then we redefine the noise so that $\sigma^2 = \sigma_n^2(1 + \sigma_{\rm struct}^2/\sigma_n^2) = 12\sigma_n^2$ to find that the structure noise in the image is $\sqrt{11}$, which is roughly 3 times the random noise.

This approach does not test a priori how well the model envelope + outflow + disk fits the data. Rather, it provides a way to assign uncertainties to the model parameters, using the best-fit model as a benchmark. Defined this way, a reduced χ^2 value of 2 leads to a contour in the (σ, T, i) parameter grid (here σ means nondimensional density, not noise) that defines a reasonable parameter uncertainty range, motivated because, for Gaussian noise statistics, this value corresponds to a suitably large 95% confidence interval. Visual inspection of models having this value showed fits that were plausible but decidedly worse than the best-fit model.

The reduced χ^2 was a useful quantitative statistic to compare models with different parameters, but in practice it had several limitations. First, the large intensity difference between the central and outer regions meant that bright pixels, although few in number, tended to dominate the χ^2 fit. The bright pixels were down-weighted by adding a Poisson-like term to the noise, $\sigma = \sigma_n(1 + \sqrt{d_i})$ so that most pixels in the image effectively contributed to the fit. Another limitation was that high-inclination models were not ruled out by the χ^2 test, although they had the generic defect that the stellar PSF was invisible, unlike the data. Simply lowering the model optical depth to make the star visible could not cure this problem, because high-inclination models with a stellar PSF *always* showed the second (southern) outflow lobe, in contradiction to the data. Imposing the additional constraint that acceptable models must display a stellar-like PSF ruled out models with inclinations above 50°. Although it might seem surprising that high-inclination models could appear similar to the PSF, it is an established property of centrally peaked intensity profiles (Adams 1991; Terebey et al. 1993; Motte & André 2001) that a

power-law intensity convolved with the PSF will have an apparent size comparable to the PSF.

Figures 8 and 9 show the translation of nondimensional parameters σ and T into the physical parameters of inner mass and infall rate for models with acceptable fits. The physical parameters were generated by varying the disk radius from 20 to 320 AU in factor-of-2 steps and then computing the mass and infall rates implied by the parameters σ and T for all acceptable model fits. Note that the protostar mass can be plausibly restricted to between 0.1 and 1.0 $M_\odot$, given that protostars eventually become T Tauri stars, and that 0.4–0.5 $M_\odot$ is a typical T Tauri star mass.

5. RESULTS

The model-fit results provide information on the physical characteristics of TMC-1. Given that we are fitting the scattered-light distribution, the model results are primarily useful in constraining the distribution of circumstellar material. In particular, the inner mass, infall rate, and age derived from the model fits represent the cloud mass that has fallen into the inner region (star plus disk) at a rate given by the infall rate, over the time since the onset of cloud collapse. These parameters are related but probably not identical to stellar parameters. The protostar mass is often assumed to be the same as the inner mass; however, many factors can reduce the protostar accretion rate and hence the protostar mass, a point that we return to later.

Figure 8 shows that the inner mass and infall rate parameters are not independent but are correlated such that a higher inner mass implies a higher infall rate. It is useful to have a quantitative relation between mass and infall rate (Fig. 8), relative to the fiducial values $M_{\rm in} = 0.5\ M_\odot$ and $\dot{M}_{\rm in}/(5\times10^{-6}\ M_\odot\ {\rm yr}^{-1})$. The solid line shows the relation $\log[\dot{M}_{\rm in}/(5\times10^{-6}\ M_\odot\ {\rm yr}^{-1})] = 0.68\log(M_{\rm in}/0.5\ M_\odot)^{+0.34}_{-0.19}$, where the $\pm$ deviations indicate that acceptable fits differ by up to a factor of 2 from the line. No special physical significance is attributed to this relation, since the model-fitting procedure has so far only been applied to one object.

The age of the protostar is an important but very difficult to measure physical characteristic. The age of the protostar is approximately the same or somewhat shorter than the age of the collapsing cloud, since the formation of a hydrostatic central object happens very quickly after cloud collapse begins. For the TSC84 solution, $t = M_{\rm in}/\dot{M}_{\rm in}$ gives the time since the onset of gravitational cloud collapse. Figure 9 indicates that the age of TMC-1 is well constrained; namely, it is independent of the mass, infall rate, and disk radius, and has a value of 1×10^5 yr to within a factor of 2. The age is consistent with statistical estimates of ages for class I protostars and is smaller than the $\sim(1-3)\times10^6$ yr age derived for the Taurus star-forming region (Kenyon & Hartmann 1995; Simon et al. 2000; Briceno et al. 2002).

Although we express the collapse age in terms of the TSC84 model, the result should apply more generally to other types of collapse models, as can be seen from the following argument. For the slowly rotating initial cloud state assumed by TSC84, gas pressure balances gravity, and the density is close to that of the singular isothermal sphere for which $\rho = a^2/2\pi r^2$ (Shu 1977; Terebey et al. 1984). The average density inside radius r is $\langle\rho\rangle = 3\rho(r)$, and the collapse happens on the sound crossing time $t = r/a$, at which time half of the material within radius r has fallen into the inner region (protostar plus disk) and half is on its way to the center. Compare this with the free-fall time for a pressureless collapse. The free-fall time for a uniform density sphere is given by $t_{\rm ff} = (3\pi/32G\rho)^{1/2}$ (Hartmann 1998); evaluating using $\langle\rho\rangle$ above gives $t_{\rm ff} = (\pi/4)r/a$, which says $t_{\rm ff}\sim t$, namely, that the free-fall time and the sound crossing time are comparable to within a constant of order unity. In this context the collapse age is approximately the same for both cases, but the mass that has fallen into the central region differs by roughly a factor of 2, with the pressureless collapse accumulating mass more rapidly.

There is an important caveat concerning the mass infall rate. Following standard practice, we have expressed the infall rate $\dot{M}_{\rm in}$ assuming spherically symmetric infall. However, the presence of an outflow cavity decreases the infalling gas solid angle from 4π to $4\pi\cos\theta_w$. We can express this as a relative solid angle $f_\Omega = \cos\theta_w$, where $f_\Omega = 1$ for spherical infall. Hence, $\dot{M}_c = f_\Omega\dot{M}_{\rm in}$ is the current mass infall rate. For TMC-1 the derived value of θ_w depends on source inclination; the mass infall rate $\dot{M}_c$ is smaller than $\dot{M}_{\rm in}$ by $\cos\theta_w = 0.76$ for the 45° best-fit inclination. This means that the mass-infall rate for TMC-1 is about 3/4 the model values shown in Figure 8, which are expressed in terms of a spherically symmetric model.

The smaller infall rate means that the mass M_c that has fallen into the central region will be smaller as well, such that $f_\Omega\dot{M}_{\rm in}t < M_c < \dot{M}_{\rm in}t$, depending on when the outflow cavity achieved its current opening angle. For the specific assumption that f_Ω decreases linearly with time from an initial value of 1 (i.e., no outflow cavity at $t = 0$), then $M_c = \bar{f}_\Omega\dot{M}_{\rm in}t$, where $\bar{f}_\Omega = (1+f_\Omega)/2$ is the time average value and where $\bar{f}_\Omega = 0.88$ for TMC-1 for the best-fit inclination. Previous studies do not include this correction, in part because the assumed wind opening angle is smaller than what we measure here for TMC-1, but the factor should be applied in principle to all $\dot{M}_c$ that are derived from radiative-scattering models.

The disk radius is not highly constrained by the NICMOS data, except to conclude that disks with radii larger than 160 AU do not produce acceptable fits. Visually, small disks lead to models with very centrally peaked intensity profiles, similar to the data. The models with large disks and flattened envelopes (§ 4) produce intensity versus radius profiles that are too shallow.

In our solutions the mass and infall rate are not independent but correlated. To further restrict the parameter values requires an independent constraint. One possible constraint is the value of the effective sound speed a for the TMC-1 core. The effective sound speed, estimated from the line width of ammonia or other high-density tracer, is a way to characterize the contribution of magnetic fields and turbulence to the pressure support of a dense cloud core, over and above that provided by thermal pressure support. We were unable to find relevant molecular-line data at the position of the TMC-1/IRAS 04381+2540 source. Instead, we use the thermal sound speed $a = 0.19$ km s^{-1}, based on 10 K gas found in Taurus dense cores by Myers & Benson (1983) at a number of locations. This value for the sound speed corresponds to a spherical mass infall rate of $1.6\times10^{-6}\ M_\odot\ {\rm yr}^{-1}$, whereas a sound speed value $a = 0.28$ km s^{-1} corresponds to $5.0\times10^{-6}\ M_\odot\ {\rm yr}^{-1}$, the same as our fiducial model. If we assume the sound speed is close to the thermal sound speed value of 0.19 km s^{-1}, then Figure 8 shows the closest corresponding acceptable fit model is for $0.125\ M_\odot$ and $\dot{M}_{\rm in} = 1.77\times10^{-6}\ M_\odot\ {\rm yr}^{-1}$. In addition, the age is $t = 7\times10^4$ yr, inclination $i = 45°$, the expansion wavefront $r = at = 21'' = 2900$ AU, and cloud radius $R = 49'' = 6900$ AU. Applying the infall solid-angle factor f_Ω leads to a current (nonspherical) infall rate $\dot{M}_c = 1.35\times10^{-6}\ M_\odot\ {\rm yr}^{-1}$ and inner mass range 0.096–0.125 $M_\odot$, where the inner mass is 0.11 $M_\odot$ if the infall solid angle decreases linearly with time.

Summarizing several millimeter-continuum results, the mass of the TMC-1 envelope is 0.16 and 0.59 $M_\odot$ for radii of 3900 and 12,000 AU, respectively (Motte & André 2001; Hogerheijde & Sandell 2000). The corresponding envelope mass for the TSC84 model above is 0.17–0.22 and 0.7–0.9 $M_\odot$, where the mass

range depends on the wind solid angle, as described. Here we assume the inner mass does not contribute to the millimeter emission, because it has been either incorporated into one or two protostars or expelled by their outflows. The agreement between our near-infrared model and the millimeter-continuum data seems reasonable, given the very different wavelengths and spatial resolutions.

In previous work, Whitney et al. (1997) fit global parameters for Taurus sources, such as near-infrared colors and polarization, rather than trying to fit detailed source structure. They restricted their scattering models to narrow wind opening angles and quote a best fit for TMC-1 of $\theta_w = 11^\circ$ and $i = 60^\circ - 72^\circ$, which is inconsistent with the structure visible in our high-sensitivity data. However, their other parameters, $\dot{M} = 5 \times 10^{-6}\ M_\odot\ \mathrm{yr}^{-1}$ and $r_d = 50$ AU, are similar to values in our allowed range.

The CO molecular outflow maps of Chandler et al. (1996) also show conical outflow structure, from which they determined an inclination range $i = 40^\circ - 70^\circ$, which is consistent with our $i = 40^\circ - 50^\circ$ values. However, the projected CO outflow cone is smaller, only 20° compared with 50° in the *HST* near-infrared image. This suggests that the CO outflow structure traces higher velocity material than the wider angle near-infrared outflow. Low-velocity gas at the edges of the outflow might indicate that entrainment of envelope material into the outflow is an important process.

6. DISCUSSION

The modest 0.7 $L_\odot$ bolometric luminosity for TMC-1 could, in principle, correspond to an early stage of protostar formation, for which the inner mass is small and the luminosity is mostly accretion luminosity, $L_{\rm acc}$, or to a later stage consistent with a roughly 1 $M_\odot$ T Tauri star with luminosity L_* and little accretion luminosity. Spectroscopically, TMC-1 and other similar class I sources are featureless (Luhman 2004; White & Hillenbrand 2004), suggesting active accretion and a young evolutionary stage.

We consider whether the source luminosity provides a useful constraint that can narrow the range of acceptable parameters. The accretion luminosity is $GM_*\dot{M}_*/R_*$ for a steady state and has a predicted value of about 8 $L_\odot$ for the "typical" protostar parameters $M_* = 0.5\ M_\odot$, $R_* = 3\ R_\odot$, and $\dot{M}_* = 1.6 \times 10^{-6}\ M_\odot\ \mathrm{yr}^{-1}$ (Hartmann 1998). In the case of TMC-1, assuming $M_* = f_\Omega M_{\rm in}$ and $\dot{M}_* = f_\Omega \dot{M}_{\rm in}$, the 10 K gas model with $M_* \sim 0.1\ M_\odot$ and $\dot{M}_* = 1.35 \times 10^{-6}\ M_\odot\ \mathrm{yr}^{-1}$ leads to a plausible value of $L_{\rm acc} \sim 1.4\ L_\odot$, about a factor of 2 higher than the bolometric luminosity. However, the fiducial model gives protostellar values $M_* = 0.44\ M_\odot$ and $\dot{M}_* = 3.8 \times 10^{-6}\ M_\odot\ \mathrm{yr}^{-1}$ that lead to an accretion luminosity of about 17 $L_\odot$, a value much higher than is observed.

As discussed by Hartmann (1998) and others, there is a long-standing problem that the expected 8 $L_\odot$ accretion luminosity is higher than the $\sim$1 $L_\odot$ characteristic observed value. Previously proposed explanations lower the stellar accretion rate and hence the accretion luminosity by considering that (1) the accretion rate through the disk may be time variable, or (2) some of the accreting disk material may be redirected into the outflow and never reach the star (Bontemps et al. 1996; Hartmann 1998; Shu et al. 1996; Motte & André 2001). The luminosity mismatch indicates that it is too simplistic to assume that the stellar accretion rate and stellar mass are given directly by the mass infall rate derived from the collapsing cloud core (i.e., circumstellar envelope).

We generalize this idea by using efficiency factors for important processes. Let the accretion rate onto a given protostar be defined as $\dot{M}_* = f_m \dot{M}_{\rm in}$, where $f_m = f_* \times f_b \times f_\Omega$ gives the mass accretion rate efficiency. The protostellar wind redirects some of the accreting disk material directly into the wind; f_* ranges from 2/3 to 1 for various wind models (Pelletier & Pudritz 1992; Wardle & Konigl 1993; Shu et al. 1996). Protobinary systems are common; if, for example, the mass infall is split equally between two components, then $f_b = 0.5$ for one component. Finally, f_Ω, defined in § 5, is a geometric factor that describes how the 4π solid angle is apportioned between the infall and wind. Assuming $f_* = 2/3$ (Shu et al. 1996), $f_b = 0.5$, and $f_\Omega = 0.76$ gives $f_m = 0.25$, so the current accretion rate onto the specified protostar is 1/4 the initial $\dot{M}_{\rm in}$, recalling that $\dot{M}_{\rm in} = 0.975a^3/G$ is the spherically symmetric infall rate into the inner region when the cloud first started to collapse.

The protostellar mass is related to the infall rate by $M_* = \int f_m \dot{M}_{\rm in}\, dt$, where f_m varies with time. We assume $f_* = 2/3$ is constant with time, so that there is always a 2:1 ratio of stellar accretion to wind outflow. We also assume accretion onto a binary companion started recently, so that $f_b = 1.0$ is a good approximation of the time behavior. The choice $f_b = 0.5$ is also reasonable, but for our purpose $f_b = 1.0$ is used because it leads to the maximum plausible mass for an individual object. Furthermore, assume as before that f_Ω decreases linearly with time to obtain $M_* = \bar{f}_m \dot{M}_{\rm in} t = \bar{f}_m M_{\rm in}$, where $\bar{f}_m = f_* \times f_b \times \bar{f}_\Omega = 0.59$ so that the protostellar mass obtains roughly 60% of the value it would have from assuming steady infall at the initial rate.

In steady state, the accretion luminosity is given by $L_{\rm acc} = f_{\rm acc} GM_{\rm in}\dot{M}_{\rm in}/R_*$ with $f_{\rm acc} = f_x \times \bar{f}_m \times f_m$, where the additional factor f_x accounts for the efficiency of energy deposition onto the star. We consider whether our fiducial model can be made consistent with the luminosity constraint. Using $f_m = 0.25$ and $\bar{f}_m = 0.59$ from above and $f_x = 0.62$ (Shu et al. 1996) gives $f_{\rm acc} = 0.091$ and reduces the accretion luminosity to just under 2.4 $L_\odot$, a value still greater than what is observed. If we take the maximum plausible value of the accretion luminosity to be 1 $L_\odot$, then the luminosity constraint, combined with the relation for acceptable fits shown in Figure 8, rules out scattering models that have $\dot{M}_{\rm in} > 3.5 \times 10^{-6}\ M_\odot\ \mathrm{yr}^{-1}$ for the infall rate and >0.3 $M_\odot$ for the inner mass. This implies that 0.18 $M_\odot$ is the maximum protostellar mass and that $0.88 \times 10^{-6}\ M_\odot\ \mathrm{yr}^{-1}$ is the corresponding accretion rate onto the protostar. The application of a luminosity constraint rules out much of the parameter space in Figure 8 and implies a maximum inner mass of 0.3 $M_\odot$, which is somewhat higher than the 0.12 $M_\odot$ inner mass previously derived assuming 10 K gas in the cloud. The introduction of less-than-unity efficiency factors means that the protostar mass is smaller than the cloud mass that has fallen into the central (inner) region. This has the important consequence that the timescale to reach a given protostar mass is longer than the value $t = M_{\rm in}/\dot{M}_{\rm in}$ that is commonly assumed.

7. SUMMARY

We present high spatial resolution *HST* NICMOS images of the class I protostar TMC-1/IRAS 04381+2540 at 1.6 μm wavelength. The near-infrared nebulosity shows a conical outflow cone with a 50° apparent semiopening angle. In addition, a jet is seen to extend north from the protostar. The position angle of the jet differs by about 5° from the position angle of the wide-angle outflow. The data show that the projected opening angle of the near-infrared outflow cavity is significantly larger than previous measurements of the CO outflow opening angle. The geometry of the outflow resembles a cone of radius R inclined toward the observer, such that the near edge of the outflow cone appears highly foreshortened.

We generate a grid of Monte Carlo scattering models for comparison with the data. The density of the envelope is taken to

be the TSC84 collapse model. A geometrically thin disk and evacuated outflow cavity are also included. Comparison of the radiative transfer models with the data shows good agreement in explaining the main features of the scattered-light distribution. The best-fit model that minimizes the reduced χ^2 has source inclination $i = 45^\circ$, deprojected wind semiopening angle $\theta_w = 40^\circ$, and nondimensional parameters $\sigma = 0.42$ and $T = 0.12$; the nondimensional parameters σ and T correspond to a family of different masses, infall rates, and disk radii. We define a χ^2 surface to represent models that give acceptable fits.

This paper represents an advance in understanding the interrelationship of parameters and uniqueness of fits for radiative transfer models. For TMC-1 the model fitting shows that the mass and infall rate parameters are not independent but are correlated such that a higher inner mass implies a higher infall rate, described by the approximate relation $\log [\dot{M}/(5 \times 10^{-6}\ M_\odot\ \mathrm{yr}^{-1})] = 0.68 \log (M/0.5\ M_\odot)^{+0.34}_{-0.19}$, where the $\pm$ deviations indicate that acceptable fits differ by up to a factor of 2 from the line. The disk radius is not highly constrained by the NICMOS data, except to conclude that disks with radii larger than 160 AU do not produce acceptable fits.

The results of our scattering models indicate that the age of TMC-1, namely, the time since cloud collapse began, is well constrained in that the age is independent of the mass, infall rate, and disk radius and has a value of 1×10^5 yr to within a factor of 2. This result is not sensitive to the assumed collapse model. The derived age is consistent with statistical estimates of ages for class I protostars and is smaller than the $\sim 1-3 \times 10^6$ yr age of the Taurus star-forming region.

We introduce efficiency factors to describe how the protostar mass is likely to be smaller than the total mass reservoir that has fallen into the inner region. Plausible efficiency factors give an accretion luminosity that is consistent with the 0.7 $L_\odot$ observed luminosity. Assuming that the luminosity is dominated by steady-state accretion, the estimated mass of the protostar ranges from about 0.1 $M_\odot$ for high efficiency to 0.2 $M_\odot$ for low accretion efficiency onto the protostar. Similarly, the estimated mass accretion rate *onto the protostar* ranges from roughly 0.9×10^{-6} to $1.4 \times 10^{-6}\ M_\odot\ \mathrm{yr}^{-1}$, which is smaller than the $(1.6-3.5) \times 10^{-6}\ M_\odot\ \mathrm{yr}^{-1}$ infall rate *of the cloud*. If low efficiency rates are prevalent for protostars, one important consequence is that it will take longer to assemble the central star than the time $t = M_{\mathrm{in}}/\dot{M}_{\mathrm{in}}$, a time that assumes *all* of the infalling mass lands on the protostar.

Future work that independently determines the mass of the central protostar would help test whether the luminosity constraint outlined in this paper is a useful assumption for protostars in the class I phase. Additional theoretical work will be needed in order to derive realistic efficiency factors and to predict protostar luminosities.

S. T. gratefully acknowledges support by grants from the Space Telescope Science Institute and by the National Aeronautics and Space Administration. We thank the referee for helpful comments.

Facilities: HST (NICMOS).

REFERENCES

Adams, F. C. 1991, ApJ, 382, 544
Bontemps, S., André, P., Terebey, S., & Cabrit, S. 1996, A&A, 311, 858
Briceno, C., Luhman, K. L., Hartmann, L., Stauffer, J. R., & Kirkpatrick, J. K. 2002, ApJ, 580, 317
Burrows, C. J., et al. 1996, ApJ, 473, 437
Casertano, S., Jedrzejewski, R., Keyes, T., & Stevens, M., eds. 1997, The 1997 *HST* Calibration Workshop with a New Generation of Instruments (Baltimore: STScI)
Chandler, C. J., & Richer, J. S. 2000, ApJ, 530, 851
Chandler, C. J., Terebey, S., Barsony, M., Moore, T. J. T., & Gautier, T. N. 1996, ApJ, 471, 308
Chen, H., Myers, P. C., Ladd, E. F., & Wood, D. O. S. 1995, ApJ, 445, 377
Davis, C. J., Mundt, R., Ray, T. P., & Eisloffel, J. 1995, AJ, 110, 766
Eisloffel, J., & Mundt, R. 1998, AJ, 115, 1554
Grosso, N., Alves, J., Wood, K., Neuhauser, R., Montmerle, T., & Bjorkman, J. E. 2003, ApJ, 586, 296
Hartmann, L. W. 1998, Accretion Processes in Star Formation (Cambridge: Cambridge Univ. Press), chap. 4
Heyer, M. H., Ladd, E. F., Myers, P. C., & Campbell, B. 1990, AJ, 99, 1585
Hogerheijde, M. R., & Sandell, G. 2000, ApJ, 534, 880
Hogerheijde, M. R., Van Dishoeck, E. F., Blake, G. A., & Van Langevelde, H. J. 1998, ApJ, 502, 315
Kenyon, S. J., Calvet, N., & Hartmann, L. W. 1993a, ApJ, 414, 676
Kenyon, S. J., & Hartmann, L. 1995, ApJS, 101, 117
Kenyon, S. J., Whitney, B. A., Gomez, M., & Hartmann, L. 1993b, ApJ, 414, 773
Kim, S.-H., Martin, P. G., & Henry, P. D. 1994, ApJ, 422, 164
Krist, J., & Hook, R. N. 1997, in The 1997 *HST* Calibration Workshop with a New Generation of Instruments, ed. S. Casertano et al. (Baltimore: STScI), 192
Lucas, P. W., & Roche, P. F. 1998, MNRAS, 299, 699
Luhman, K. L. 2004, ApJ, 617, 1216
Motte, F., & André, P. 2001, A&A, 365, 440
Myers, P. C., & Benson, P. J. 1983, ApJ, 266, 309
Pelletier, G., & Pudritz, R. E. 1992, ApJ, 394, 117
Shu, F. H. 1977, ApJ, 214, 488
Shu, F. H., Adams, F., & Lizano, S. 1987, ARA&A, 25, 23
Shu, F. H., Shang, H., & Lee, T. 1996, Science, 271, 1545
Simon, M., Dutrey, A., & Guilloteau, S. 2000, ApJ, 545, 1034
Stahler, S. W. 1988, ApJ, 332, 804
Terebey, S., Chandler, C. J., & André, P. 1993, ApJ, 414, 759
Terebey, S., Shu, F. H., & Cassen, P. 1984, ApJ, 286, 529 (TSC84)
Terebey, S., Van Buren, D., Hancock, T., Padgett, D. L., & Brundage, M. 2001, in ASP Conf. Ser. 243, From Darkness to Light, ed. T. Montmerle & P. André (San Francisco: ASP), 243
Wardle, M., & Konigl, A. 1993, ApJ, 410, 218
White, R. J., & Hillenbrand, L. A. 2004, ApJ, 616, 998
Whitney, B. A., & Hartmann, L. 1993, ApJ, 402, 605 (WH93)
Whitney, B. A., Kenyon, S. J., & Gómez, M. 1997, ApJ, 485, 703
Whitney, B. A., Wood, K., Bjorkman, J. E., & Wolff, M. 2003, ApJ, 591, 1049
Wolf, S., Padgett, D. L., & Stapelfeldt, K. R. 2003, ApJ, 588, 373